

RVFL-X: A Novel Randomized Network Based on Complex Transformed Real-Valued Tabular Datasets

M. Sajid

Department of Mathematics

Indian Institute of Technology Indore, India
phd2101241003@iiti.ac.in

Mushir Akhtar

Department of Mathematics

Indian Institute of Technology Indore, India
phd2101241004@iiti.ac.in

A. Quadir

Department of Mathematics

Indian Institute of Technology Indore, India
mscphd2207141002@iiti.ac.in

M. Tanveer

Department of Mathematics

Indian Institute of Technology Indore, India
mtanveer@iiti.ac.in

Abstract—Recent advancements in neural networks, supported by foundational theoretical insights, emphasize the superior representational power of complex numbers. However, their adoption in randomized neural networks (RNNs) has been limited due to the lack of effective methods for transforming real-valued tabular datasets into complex-valued representations. To address this limitation, we propose two methods for generating complex-valued representations from real-valued datasets: a natural transformation and an autoencoder-driven method. Building on these mechanisms, we propose RVFL-X, a complex-valued extension of the random vector functional link (RVFL) network. RVFL-X integrates complex transformations into real-valued datasets while maintaining the simplicity and efficiency of the original RVFL architecture. By leveraging complex components such as input, weights, and activation functions, RVFL-X processes complex representations and produces real-valued outputs. Comprehensive evaluations on 80 real-valued UCI datasets demonstrate that RVFL-X consistently outperforms both the original RVFL and state-of-the-art (SOTA) RNN variants, showcasing its robustness and effectiveness across diverse application domains.

Index Terms—Randomized neural network (RNN), Random vector functional link (RVFL), Extreme learning machine (ELM), Complex-valued, Real-valued, Autoencoder, Neuro-Fuzzy.

I. INTRODUCTION

THE exceptional capability of artificial neural networks (ANNs) to approximate intricate nonlinear mappings has established them as a pivotal tool across a wide spectrum of machine learning applications [1]. ANNs have demonstrated substantial success in diverse domains, including autonomous driving [2], Alzheimer's disease diagnosis [3], [4], [5], Protein structure prediction [6] etc.

The backpropagation (BP) algorithm, underpinned by gradient descent (GD), is a widely employed method for optimizing ANN parameters by minimizing the discrepancy between predicted and observed outputs. Despite its widespread use, BP-based optimization is constrained by several limitations,

M. Sajid acknowledges the Council of Scientific and Industrial Research (CSIR), New Delhi, for providing fellowship under grants 09/1022(13847)/2022-EMR-I. The code of the paper can be accessed from <https://github.com/AnonymousAuthor0011/RVFL-X>.

including computational inefficiency, convergence to suboptimal local minima [7], and sensitivity to hyperparameter selection and initialization strategies. These challenges necessitate alternative methodologies for efficient neural network training.

Randomized neural networks (RNNs) [8] represent a paradigm shift, addressing the drawbacks associated with GD-based optimization. In RNNs, certain parameters are randomly generated and remain fixed during training, and the rest are optimized using closed-form or iterative algorithms [9].

Among the prominent architectures in the RNN, the random vector functional link (RVFL) network [10] has gained considerable attention for its simplicity and computational efficiency. The RVFL network, in particular, distinguishes itself through its direct connections between the input and output layers, which contribute to its robust performance. In the RVFL framework, the weights and biases of the hidden layer are initialized randomly and remain fixed throughout the training process. The output parameters, comprising both the direct link weights and those connecting the hidden layer to the output layer, are computed analytically using methods such as the pseudo-inverse or least squares [11]. The inclusion of direct connections serves as an implicit regularization mechanism, enhancing the network's learning efficacy and robustness [12]. The RVFL model also demonstrates rapid training capabilities alongside universal approximation properties [13].

The RVFL network and its advanced variants have proven effective across various domains, such as handling class imbalance [14] and noisy datasets [15], particularly in Alzheimer's disease diagnosis [14], [15]. These models have become a go-to solution due to their simplicity, efficiency, and versatility in addressing diverse challenges. However, traditional RVFL models, which rely on randomization for feature transformation, often face instability issues during learning. To address these challenges, SP-RVFL [16] introduced a sparse autoencoder with l_1 -norm regularization, enabling more stable and precise learning of network parameters. In parallel, efforts to enhance interpretability led to advanced RVFL models based on granular ball and graph embedding (GB-RVFL and

GE-GB-RVFL) [17], which improve clarity and transparency of decision making, offering valuable insights into how the models make predictions. Further advancements include the neuro-fuzzy RVFL (NF-RVFL) and neuro-fuzzy ensemble deep RVFL (edRVFL-FIS) models [18, 19], which integrate human-like reasoning, thus boosting both performance and interpretability. Further, to optimize hidden node selection, IRVFL+ [20] dynamically expands hidden nodes, making the network more adaptable. Together, these innovations have made RVFL a more powerful and versatile tool in the machine learning landscape.

II. MOTIVATION AND CONTRIBUTION

The performance of RNN-based models is significantly influenced by the generation of hidden layer features, which play a critical role in the propagation of information to the output layers. In the case of the RVFL network, hidden layer features are generated through random projection. However, this random generation often fails to capture some of the nonlinear features inherent in the data, potentially limiting the model's expressiveness. Prior studies have demonstrated that augmenting RVFL variants with feature enhancement techniques [21], [22] substantially improves their performance by capturing intricate patterns and relationships in the data. Despite these advancements, the exploration of feature enhancement remains relatively nascent in the context of RVFL-based models.

Recent studies in neural networks, coupled with foundational theoretical analyses, suggest that complex numbers offer a richer representational capacity [23], [24]. They enable robust memory retrieval mechanisms while exhibiting noise-resistant properties. These benefits, however, have been underutilized in RNNs, primarily due to the lack of mechanisms to transform real tabular datasets into complex-valued representations. To address this gap, we propose the RVFL-X model—a novel extension of RVFL that integrates complex transformations into real-valued datasets while maintaining the simplicity and efficiency of the original architecture.

The use of complex parameters introduces several advantages across computational, biological, and signal processing domains. From a computational perspective, [23] demonstrated the efficiency and numerical stability of holographic reduced representations [25], which employ complex numbers for associative memory retrieval. Similarly, biologically inspired architectures have leveraged complex weights to enhance the versatility of representations. For example, [26] introduced a biologically plausible deep network using complex-valued neurons to model richer and more adaptable representations. These studies emphasize the potential of complex formulations to encode the firing rate and relative timing of neurons.

Despite these theoretical and practical advantages, most existing applications of complex-valued neural networks are restricted to datasets inherently expressed in complex forms, such as those arising from signal processing tasks. The RVFL-X model addresses this limitation by proposing a novel mechanism to transform real tabular datasets into a complex-valued

representation. This transformation allows the RVFL-X to retain the architectural simplicity of its real-valued counterpart while exploiting the rich representational capacity of complex-valued features.

To the best of our knowledge, this is the first attempt to systematically integrate complex-valued transformations into real-valued RVFL architectures. The RVFL-X maintains the core properties of the original RVFL model with minimal architectural modifications, enabling the effective capture of nuanced patterns and relationships in real-world datasets. This novel approach paves the way for exploring new avenues in RNNs and unlocking their full potential for a wide range of applications.

The primary highlights of this paper are as follows:

- A novel mechanism is introduced to transform real tabular datasets into complex-valued representations.
- Two transformation techniques are proposed: an intuitive and natural approach; and an autoencoder-based method.
- The complex variant of RVFL (RVFL-X) is developed, which converts real-valued tabular data into complex values, employs complex weights and complex activation functions and generates real-valued outputs.
- Comprehensive comparisons of RVFL-X with 10 SOTA models are conducted across diverse datasets, including binary and multiclass classification, as well as small and large-scale data.

III. RELATED WORK

This section establishes the necessary notations and provides an overview of the RVFL network, laying the groundwork for the proposed model.

A. Notations

Consider a training dataset represented as $\mathcal{Z} = \{(z_j, w_j) \mid j \in \{1, 2, \dots, k\}\}$, where $z_j \in \mathbb{R}^{1 \times r}$ corresponds to the input features, and $w_j \in \mathbb{R}^{1 \times d}$ is the associated target vector for d classes. Here, k denotes the total number of training samples, and r indicates the number of attributes. The transpose of a matrix is denoted by $(\cdot)^T$. The matrices representing the inputs and outputs are given by $Z = [z_1^T, z_2^T, \dots, z_k^T]^T$ and $W = [w_1^T, w_2^T, \dots, w_k^T]^T$, respectively.

B. RVFL Neural Network

The RVFL network, first proposed by Pao et al. [10], is a single-layer feed-forward neural network. It consists of three main components: an input layer, a hidden layer, and an output layer. A distinguishing feature of RVFL is the random initialization of the weights connecting the input to the hidden layer, as well as the biases in the hidden layer. These parameters are fixed and not updated during training. Furthermore, RVFL allows direct connections between the input layer and the output layer, enhancing its ability to model complex relationships.

Let the hidden layer contain N_h neurons. The output of the hidden layer, denoted as G_1 , is computed as follows:

$$G_1 = \sigma(ZF_w + F_b) \in \mathbb{R}^{k \times N_h}, \quad (1)$$

where $F_w \in \mathbb{R}^{r \times N_h}$ represents the randomly initialized weight matrix with values drawn uniformly from $[-1, 1]$, $F_b \in \mathbb{R}^{1 \times N_h}$ is the bias vector, and σ is the activation function.

The output layer combines the contributions from the input features and the hidden layer. Let G_2 denote the concatenated matrix of input features Z and hidden layer outputs G_1 , defined as:

$$G_2 = [Z \quad G_1]. \quad (2)$$

The output weights $\eta \in \mathbb{R}^{(r+N_h) \times d}$ are determined by solving the following optimization problem:

$$\eta_{\min} = \arg \min_{\eta} \frac{\mathcal{C}}{2} \|G_2 \eta - W\|^2 + \frac{1}{2} \|\eta\|^2, \quad (3)$$

where $\mathcal{C} > 0$ is a regularization parameter. The closed-form solution for η is given by:

$$\eta_{\min} = \begin{cases} G_2^T (G_2 G_2^T + \frac{1}{\mathcal{C}} I)^{-1} W, & \text{if } k < (r + N_h), \\ (G_2^T G_2 + \frac{1}{\mathcal{C}} I)^{-1} G_2^T W, & \text{if } k \geq (r + N_h), \end{cases} \quad (4)$$

where I is the identity matrix of an appropriate dimension. The term $\hat{W} = G_2 \eta_{\min}$ is the predicted output of the network.

IV. PROPOSED WORK

Complex-valued neural networks offer significant advantages, however their application has primarily been limited to datasets inherently expressed in complex forms. There is a gap in extending these transformations to real-valued tabular data, limiting the broader potential of neural networks in various domains. This creates an opportunity to develop a more versatile approach that leverages complex-valued representations. We propose RVFL-X, a complex-valued variant of RVFL that transforms real-valued tabular datasets into complex representations. The proposed model preserves the simplicity of the original RVFL while utilizing complex weights and activation functions to capture more intricate patterns and relationships in the data.

A. Conversion of Real-valued Data to Complex-valued Data

This section provides a detailed explanation of the proposed process used to convert real-valued data into complex-valued data. In the subsequent subsection, we apply this methodology to define our proposed RVFL-X model using the complex-converted data. To transform the real-valued tabular dataset into a complex-valued one, we propose two distinct methods: first, an intuitive and natural approach (Section IV-A1), and second, based on an autoencoder-based method (Section IV-A2).

1) **Natural Method:** For the numerical dataset Z , we define the complex dataset Z^X as follows:

$$Z^X = Z + iS, \quad (5)$$

where $S = \mathbf{0}$ is the zero matrix having the same dimension as of Z . We call it the natural method because, in the Field of complex numbers, every real number is a complex number,

and the natural way to write a real number z into a complex number is $z + i0$, where 0 is scalar zero.

2) **Autoencoder-Based Method:** In this method, the complex dataset Z^X is constructed from a numerical dataset Z as:

$$Z^X = Z + iS, \quad (6)$$

where S is a matrix of the same dimensions as Z , obtained using an autoencoder applied to Z . The autoencoder, consisting of an encoder and a decoder, transforms Z into a latent representation S , preserving key structural properties. This latent representation serves as the imaginary part of Z^X , enriching the dataset with additional information for improved modeling. This approach leverages the autoencoder's capacity to extract and preserve essential features, ensuring the complex dataset Z^X is both informative and structurally robust.

The encoder maps the input matrix Z to the latent representation \hat{S} through random weights:

$$\hat{S} = \xi(ZW), \quad (7)$$

where $W \in \mathbb{R}^{r \times r}$ is the weight matrix initialized randomly (e.g., drawn from uniform distributions), and ξ is the normalization function. The decoder reconstructs Z from S using

$$\hat{Z} = \xi(SV), \quad (8)$$

where $V \in \mathbb{R}^{r \times r}$ is the decoder weight matrix. This normalization ensures consistency in scaling during both encoding and decoding while preserving the data's structural properties.

To learn the latent representation S , the reconstruction error between Z and \hat{Z} is minimized through an ℓ_2 -regularized optimization problem, preventing overfitting. The optimization problem is formulated as:

$$V^* = \arg \min_V \frac{\mathcal{C}}{2} \|Z - \hat{S}V\|^2 + \frac{1}{2} \|V\|^2, \quad (9)$$

where \mathcal{C} is a regularization parameter. The closed-form solution for V^* is given by:

$$V^* = \begin{cases} \hat{S}^T (\hat{S} \hat{S}^T + \frac{1}{\mathcal{C}} I)^{-1} Z, & \text{if } k < r, \\ (\hat{S}^T \hat{S} + \frac{1}{\mathcal{C}} I)^{-1} \hat{S}^T Z, & \text{if } k \geq r, \end{cases} \quad (10)$$

where I represents the identity matrix.

Once V^* is computed, the latent representation S is obtained from the encoder as:

$$S = \xi \left(Z \left(\varpi V^* + (1 - \varpi) V^{*T} \right) \right), \quad (11)$$

where ϖ takes only two values, i.e., 0 or 1, thus $\varpi \in \{0, 1\}$. ϖ is tuned during training. If $\varpi = 0$, V^* does not contribute to the formation of the imaginary part S , whereas if $\varpi = 1$, V^{*T} is excluded. This latent representation effectively captures critical features of the input data in a transformed space, enhancing robustness and generalization through regularization. Consequently, this representation defines the imaginary part of the data.

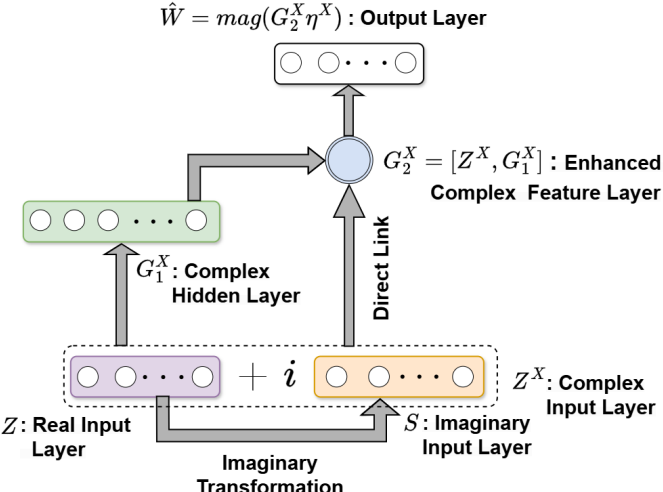


Fig. 1: Architecture of the proposed RVFL-X network.

B. RVFL-X

The architecture of the proposed RVFL-X network is depicted in Figure 1. For the given input matrix Z , we convert it to the complex version Z^X and the method of calculating it is given in Section IV-A. Let the complex weight matrix, connecting the input matrix Z^X to the hidden layer and complex bias matrix of the hidden layer be denoted as F_w^X and F_b^X , respectively, and defined as follows:

$$F_w^X = F_w^{real} + iF_w^{imag} \quad \text{and} \quad F_b^X = F_b^{real} + iF_b^{imag}, \quad (12)$$

where $F_w^{real} \in \mathbb{R}^{r \times N_h}$ and $F_w^{imag} \in \mathbb{R}^{r \times N_h}$ are generated randomly from the uniform distribution of $[-1, 1]$ space and $F_b^{real} \in \mathbb{R}^{r \times N_h}$ and $F_b^{imag} \in \mathbb{R}^{r \times N_h}$ are generated randomly from the uniform distribution of $[0, 1]$. All the columns of the F_w^{real} are identical, and similarly for F_b^{imag} .

To regularize the model from overfitting, we make some of the entries of the F_w^X and F_b^X to be zero and denoted as \hat{F}_w^X and \hat{F}_b^X , respectively. The number of entries set to be zero is regulated the hyperparameter α , where it denotes the percentage of the entries set to be zero which can be tuned during the model learning process.

The complex hidden layer is generated as follows:

$$G_1^X = \sigma^X(Z^X \cdot_X \alpha \hat{F}_w^X + _X \alpha \hat{F}_b^X) \in \mathbb{R}^{k \times N_h}, \quad (13)$$

where \cdot_X and $+_X$ are complex multiplication and addition, respectively. σ^X is modified complex activation function for the real activation function σ and defined as follows:

$$\sigma^X(z_x) = \sigma(Real(z_x)) + i\sigma(Img(z_x)), \quad (14)$$

where $Real(z^X)$ and $Img(z^X)$ are the real and imaginary part of the complex number z_x , respectively.

Next we form the enhanced feature matrix as follows:

$$G_2^X = [Z^X, G_1^X] \quad (15)$$

the predicted output \hat{W}^X of the proposed model can be

calculated as:

$$\hat{W} = mag(G_2^X \eta^X), \quad (16)$$

where η^X is the complex weight matrix connecting the enhanced feature layer (concatenation of input and hidden layers) to the output layer. $mag(z_x)$ is the magnitude of the complex number z_x and defined as $\sqrt{Real(z_x)^2 + Img(z_x)^2}$.

The proposed optimization problem can be formulated as:

$$\eta_{\min}^X = \arg \min_{\eta^X} \frac{\mathcal{C}}{2} \|G_2^X \eta^X - W\|^2 + \frac{1}{2} \|\eta^X\|^2, \quad (17)$$

where $\mathcal{C} > 0$ is a regularization parameter and same as used in (9). After solving the optimization problem (17) for η^X , we get:

$$\eta_{\min}^X = \begin{cases} (G_2^X)^T \left((G_2^X)(G_2^X)^T + \frac{1}{\mathcal{C}} I \right)^{-1} W, & \text{if } k < (r + N_h), \\ \left((G_2^X)^T (G_2^X) + \frac{1}{\mathcal{C}} I \right)^{-1} (G_2^X)^T W, & \text{if } k \geq (r + N_h). \end{cases} \quad (18)$$

As described in Section IV-A, we proposed two methods for generating the imaginary part of the data. Accordingly, the RVFL-X model based on the method in Section IV-A1 will be referred to as RVFL-X-N, while the RVFL-X model based on the method in Section IV-A2 will be denoted as RVFL-X-Auto henceforth.

V. EXPERIMENTS, RESULTS AND DISCUSSION

This section presents comprehensive details of the experimental setup, datasets, and compared models. Subsequently, we delve into the experimental results and conduct statistical analyses. At last, we conduct sensitivity analyses for various hyperparameters of the proposed RVFL-X and ablation study. The code of the paper can be accessed using the following link: <https://github.com/AnonymousAuthor0011/RVFL-X>.

A. Compared Models, Datasets and Experimental Setup

Compared Models: We conduct comparisons among the proposed RVFL-X; and several benchmarks, including RVFL [10], RVFLwoDL (RVFL without direct link, also known as extreme learning machine(ELM)) [27], intuitionistic fuzzy RVFL (IFRVFL) [15], graph embedded ELM with linear discriminant analysis (GEELM-LDA) [28], graph embedded ELM with local Fisher discriminant analysis (GEELM-LFDA) [28], Total variance RVFL (Total-var-RVFL) [29] minimum class variance based ELM (MCVELM) [30] and Neuro-fuzzy RVFL-R (NF-RVFL-R), Neuro-fuzzy RVFL-K (NF-RVFL-K), and Neuro-fuzzy RVFL-C (NF-RVFL-C) whose fuzzy layer centers are generated using random-means, K-means and fuzzy C-means [18].

Datasets: To assess the effectiveness of the proposed RVFL-X models, we utilize 80 benchmark datasets from the UCI repository [31], spanning various domains and sizes. These datasets are categorized into four groups: C-1 category: binary and small, C-2 category: binary and large, C-3 category: multiclass and small, and C-4 category: multiclass and large.

TABLE I: Average accuracy and rank across 21 C-1 category datasets.

Metric ↓ Model →	RVFL [10]	RVFLwoDL [27]	IFRVFL [15]	GEELM-LDA [28]	GEELM-LFDA [28]	Total-var-RVFL [29]	MCVELM [30]	NF-RVFL-R [18]	NF-RVFL-K [18]	NF-RVFL-C [18]	RVFL-X-N [†]	RVFL-X-Auto [†]
Average Accuracy	79.993	79.7806	80.3335	75.703	72.4096	81.1158	80.9615	80.6137	80.884	81.6269	<u>82.6226</u>	82.8618
Average Rank	8.2381	8.9048	6.2381	9.3571	10.5714	5.5	5.5	5.6905	5.5714	5.2619	<u>4.5</u>	2.6667

The bold values in each row indicate the best-performing model w.r.t. to the row metric, while the underlined values highlight the second-best-performing model. [†] denotes the proposed models.

TABLE II: Average accuracy, rank and standard deviation (Std. Dev.) across 14 C-2 category datasets.

Metric ↓ Model →	RVFL [10]	RVFLwoDL [27]	IFRVFL [15]	GEELM-LDA [28]	GEELM-LFDA [28]	Total-var-RVFL [29]	MCVELM [30]	NF-RVFL-R [18]	NF-RVFL-K [18]	NF-RVFL-C [18]	RVFL-X-N [†]	RVFL-X-Auto [†]
Average Accuracy	80.9677	80.0556	78.3954	79.9994	76.5356	81.5687	80.9891	80.971	81.2448	81.6908	<u>82.1302</u>	83.3793
Average Rank	7.2857	9.5714	10.8571	8.2143	8.1071	4.6071	6.5	7.3214	6.5	4.1429	<u>2.8214</u>	2.0714
Average Std. Dvn.	4.4417	4.7219	5.2407	5.3081	10.0387	4.7577	4.4265	4.8611	4.6659	4.9101	4.3711	<u>4.4173</u>

The bold values in each row indicate the best-performing model w.r.t. to the row metric, while the underlined values highlight the second-best-performing model. [†] denotes the proposed models.

Small datasets have sample sizes ranging from 100 to 1,000, while large datasets range from 1,001 to 100,000.

Experimental Setup: The experimental hardware setup includes a personal computer equipped with an Intel(R) Xeon(R) Gold 6226R CPU, operating at a clock speed of 2.90 GHz, and 128 GB of RAM. The system runs Windows 11 and utilizes Matlab 2023a to execute all experiments. Following the experimental protocol in [18], we determine the optimal hyperparameters and testing accuracy using grid search along with a five-fold cross-validation technique. Additionally, the hyperparameters for all baseline models are tuned according to the approach outlined in [18]. For the baseline models, we tune six activation functions: (1) Sigmoid, (2) Sine, (3) Tribas, (4) Radbas, (5) Tansig, and (6) ReLU, as specified in [18]. For the proposed RVFL-X model, real-valued activation functions are transformed into complex activation functions using the method described in Section IV-B of the main manuscript. The regularization parameter \mathcal{C} is chosen from the range $\{10^{-5}, 10^{-4}, \dots, 10^5\}$. The number of hidden nodes (N) is selected from the range of 3 to 203, with a step size of 20. For the proposed model, the percentage parameter (α) is tuned from the set $\{0, 0.1, \dots, 0.5\}$, where $\alpha = t$ represents the $t \times 100$ percentage that sets the parameters to zero, as discussed in Section IV-B.

B. Evaluation on C-1 Category Datasets

Table I summarizes the experimental results, showcasing the average Average accuracy and rank of the proposed RVFL-X models compared to baseline models across 21 C-1 category (binary and small) datasets. A complete accuracy table for each model on each dataset is provided in Table VII of the Appendix. Among them, the proposed RVFL-X-Auto achieves the highest average accuracy of 82.8618%, followed by the proposed RVFL-X-N at 82.6226%, outperforming other SOTA models.

Average accuracy can be misleading as it may hide variations in a model's performance across datasets. To address this, we followed Demšar [32] and conducted statistical tests, including the statistical ranking, Friedman test, and Nemenyi post hoc test. These tests ensured unbiased performance evaluation and enabled broader conclusions about model effectiveness. In the ranking approach, models are ranked based on their dataset-wise performance, with lower ranks for better models. Let \mathcal{S} and \mathcal{R} represent the number of models and

datasets, respectively. The rank of the s^{th} model on the r^{th} dataset is $\rho(s, r)$, and its average rank is calculated as $\rho(s, *) = \frac{1}{\mathcal{R}} \sum_{r=1}^{\mathcal{R}} \rho(s, r)$. The last row of Table I shows average ranks, where the proposed RVFL-X-Aut, and RVFL-X models, with ranks 2.6667 and 4.5, respectively, outperform baseline models.

The Friedman test [33] compares models' average ranks to identify significant differences. It uses the chi-squared statistic χ_F^2 with $\mathcal{S} - 1$ degrees of freedom (dof): $\chi_F^2 = \frac{12\mathcal{R}}{\mathcal{S}(\mathcal{S}+1)} \left(\sum_{s=1}^{\mathcal{S}} \rho(s, *)^2 - \frac{\mathcal{S}(\mathcal{S}+1)^2}{4} \right)$. Iman and Davenport [34] improved χ_F^2 with the F_F statistic: $F_F = \chi_F^2 \cdot \frac{(\mathcal{R}-1)}{\mathcal{R}(\mathcal{S}-1)-\chi_F^2}$. The distribution of F_F is characterized by $(\mathcal{S}-1)$ and $(\mathcal{R}-1)(\mathcal{S}-1)$ dof. For $\mathcal{S} = 12$ and $\mathcal{R} = 21$, $\chi_F^2 = 92.653$ and $F_F = 13.3943$. The F -distribution table shows $F_F(11, 220) = 1.8324$ at a 5% significance level. Since $13.3943 > 1.8324$, we reject the null hypothesis, confirming significant differences among the models.

Further, the Nemenyi post hoc test [32] evaluates pairwise statistical differences between models. If the average rank of model s_1 is lower than that of s_2 by at least the critical difference (C.D.), s_1 is deemed statistically superior. The C.D. is computed as $C.D. = q_{\alpha} \sqrt{\frac{\mathcal{S}(\mathcal{S}+1)}{6\mathcal{R}}}$, where q_{α} is the critical value from [32]. At $\alpha = 0.05$, $C.D. = 3.6363$. Based on the ranks in Table I, both the proposed RVFL-X models are statistically superior to RVFL, RVFLwoDL, GEELM-LDA, and GEELM-LFDA. However, the test fails to establish statistical differences between the proposed models and other baseline methods. Nevertheless, the lowest rank and highest accuracy of the proposed models compared to all existing SOTA models confirm their superior generalization capabilities.

C. Evaluation on C-2 Category Datasets

Table II presents the experimental results, including the average accuracy, standard deviation, and rank of the proposed RVFL-X models compared to baseline models across 14 C-2 category (binary and large) datasets. Detailed accuracy for each model on individual datasets is provided in Table VIII of the Appendix.

From the results, the RVFL-X-Auto model demonstrates the highest accuracy (83.3793%), the lowest standard deviation (2.0714), and the second-lowest rank (4.4173). This highlights the model's ability to effectively transform real-valued datasets

TABLE III: Average accuracy and rank across 23 C-3 category datasets.

Metric ↓ Model →	RVFL [10]	RVFLwoDL [27]	Total-var-RVFL [29]	MCVELM [30]	NF-RVFL-R [18]	NF-RVFL-K [18]	NF-RVFL-C [18]	RVFL-X-N [†]	RVFL-X-Auto [†]
Average Accuracy	71.385	70.9367	70.9649	71.203	71.6119	72.0101	72.137	<u>73.2906</u>	74.119
Average Rank	6.3478	7.2826	5.2391	5.4783	5.8478	5.1957	4.6522	<u>2.6739</u>	2.2826

The bold values in each row indicate the best-performing model w.r.t. to the row metric, while the underlined values highlight the second-best-performing model. [†] denotes the proposed models.

TABLE IV: Average accuracy, rank and standard deviation (Std. Dev.) across 22 C-4 category datasets.

Metric ↓ Model →	RVFL [10]	RVFLwoDL [27]	Total-var-RVFL [29]	MCVELM [30]	NF-RVFL-R [18]	NF-RVFL-K [18]	NF-RVFL-C [18]	RVFL-X-N [†]	RVFL-X-Auto [†]
Average Accuracy	85.3395	84.5917	84.9419	84.3676	82.7576	83.1052	85.3942	86.6683	<u>86.6252</u>
Average Rank	5.2727	7.0227	4.2727	6	7.5909	6.8409	4.5	<u>1.7955</u>	1.7045
Average Std. Dvn.	<u>2.8274</u>	3.0834	4.0949	4.1645	3.0201	3.3523	3.1336	2.9423	2.8087

The bold values in each row indicate the best-performing model w.r.t. to the row metric, while the underlined values highlight the second-best-performing model. [†] denotes the proposed models.

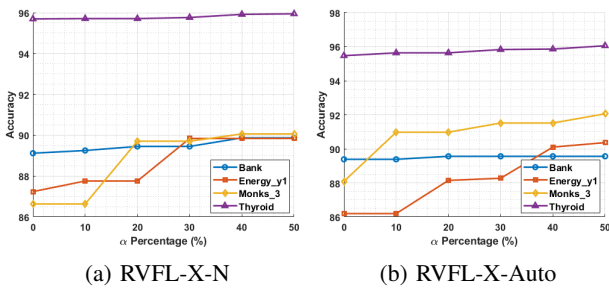


Fig. 2: Sensitivity analyses of the proposed RVFL-X-N and RVFL-X-Auto models w.r.t. α .

and process them through the complex architecture of the RVFL network. Notably, the RVFL-X-Auto and RVFL-X-N models achieve approximately 3% higher accuracy than the RVFL and RVFLwoDL networks, further confirming the superior generalization performance of the proposed RVFL-X models. Similarly, the RVFL-X-N model emerges as the second-best in accuracy while achieving the best rank, demonstrating its competitive performance. The low standard deviations of both models reflect the high certainty and stability of their predictions.

Applying the Friedman test yields $F_F = 15.3871$. Referring to the F -distribution table, with $F_F(11, 143) = 1.8562$ at a 5% significance level, we reject the null hypothesis, confirming significant differences among the models. Furthermore, the Nemenyi post hoc test calculates a critical difference ($C.D.$) of 4.4535, indicating that both proposed RVFL-X models are statistically superior to RVFL, RVFLwoDL, IF-RVFL, GEELM-LDA, GEELM-LFDA, and NF-RVFL-R.

Thus the highest accuracy, lowest standard deviation, and superior rankings of the RVFL-X-Auto and RVFL-X-N models demonstrate their exceptional generalization performance. This can be attributed to the proposed RVFL-X models' ability to exploit the rich representational capacity of complex-valued features, which enhances their predictive capabilities compared to existing baseline models.

D. Evaluation on C-3 Category Datasets

Table III summarizes the experimental results, presenting the average Average accuracy and rank of the proposed RVFL-X models compared to baseline models across 23 C-3 category (multiclass and small) datasets. Detailed results for each model for every dataset are provided in Table IX of the Appendix.

The RVFL-X-Auto and RVFL-X-N models achieve the highest and second-highest accuracies, 74.119% and 73.2906%, respectively, surpassing all baseline models. Notably, the proposed models outperform the NF-RVFL models (a recent SOTA approach leveraging an IF-THEN human-like methodology) by approximately 1%. This highlights the remarkable effectiveness of the proposed models.

In terms of rank, RVFL-X-Auto and RVFL-X-N secure the lowest and second-lowest ranks, 2.2826 and 2.6739, respectively, further validating their superior performance. The Friedman test ($F_F = 11.8338 > F_F(11, 143) = 1.9913$ at $\alpha = 0.05$) confirms significant differences among all models on these datasets. Additionally, the Nemenyi post hoc test ($C.D. = 2.5051$) reveals that the proposed RVFL-X models are statistically superior to all baseline models except NF-RVFL-C. However, the proposed models achieve lower ranks than NF-RVFL-C, emphasizing their strong generalization capability and consistent performance across diverse datasets.

E. Evaluation on C-4 Category Datasets

Table IV presents the experimental results, including the average accuracy, standard deviation, and rank of the proposed RVFL-X models compared to baseline models across 22 C-4 category (multiclass and large) datasets. Detailed results for each model w.r.t. every dataset are available in Table X of the Appendix.

The proposed RVFL-X-N model achieves the highest accuracy of 86.6683%, followed closely by RVFL-X-Auto with 86.6252%. In terms of standard deviation and rank, RVFL-X-Auto demonstrates the lowest average standard deviation and rank among all models. The Friedman test ($F_F = 34.2013 > F_F(11, 143) = 1.9939$ at $\alpha = 0.05$) and the Nemenyi post hoc test ($C.D. = 2.5614$) further confirm that the proposed models are statistically superior to all baseline models, except Total-Var-RVFL. Nevertheless, the lowest ranks of the proposed models highlight their superior generalization and adaptability.

TABLE V: Ablation Study of the RVFL-X-N Model

Proposed Variant/Dataset	bank	energy_y1	monks_3	thyroid
RVFL-X-N	89.8475	91.7927	92.9615	96.0417
RVFL-X-N _{$\alpha=0$}	89.1175	87.2371	86.6323	95.6944
RVFL-X-N-woDL	89.6042	89.9711	89.8886	95.9028
RVFL-X-N-woDL _{$\alpha=0$}	89.2502	86.0682	87.3530	95.4722

TABLE VI: Ablation Study of the RVFL-X-Auto Model

Proposed Variant/Dataset	bank	energy_y1	monks_3	thyroid
RVFL-X-Auto	89.8032	90.7555	93.1433	96.0278
RVFL-X-Auto _{$\alpha=0$}	89.3829	86.1930	88.0868	95.4722
RVFL-X-Auto-woDL	89.4050	90.4940	91.3333	95.8750
RVFL-X-Auto-woDL _{$\alpha=0$}	89.2723	86.4536	88.4472	95.5000

Notably, the RVFL-X models consistently outperform RVFLwoDL (ELM) in terms of rank and standard deviation, emphasizing the critical role of the direct link in enhancing model performance and stability.

F. Sensitivity Analysis

Sensitivity analyses of the proposed RVFL-X-N and RVFL-X-Auto models are conducted w.r.t. the percentage parameter α , which controls the proportion of zeros in the hidden layer weights and bias matrices for regularization. The results, shown in Fig. 2 for four datasets across all categories, illustrate the impact of α values ranging from 0% to 50%.

As α increases, the accuracy of both models improves, demonstrating the effectiveness of regularization through sparsity in the weight and bias matrices. Notably, accuracy stabilizes beyond a certain point, indicating that increasing α beyond this threshold does not yield additional benefits. For instance, when $\alpha = 0.5$, the models achieve near-optimal performance, highlighting this value as a practical choice for maximizing accuracy in the proposed RVFL-X models.

G. Ablation Study

An ablation study is conducted to evaluate the importance of different components in the proposed RVFL-X models. The results are summarized in Table V and Table VI for RVFL-X-N and RVFL-X-Auto, respectively. In this study, RVFL-X-N with $\alpha = 0$ (indicating no sparsity) is denoted as RVFL-X-N _{$\alpha=0$} , RVFL-X-N without the direct link is referred to as RVFL-X-N-woDL, and RVFL-X-N without the direct link and with $\alpha = 0$ is labeled as RVFL-X-N-woDL _{$\alpha=0$} . A similar nomenclature is used for RVFL-X-Auto variants.

The results demonstrate that the complete versions of RVFL-X-N and RVFL-X-Auto, which include sparsity controlled by the parameter α and incorporate the direct link, consistently outperform their respective ablated variants. This highlights the critical role of sparsity in weights and biases, as well as the inclusion of the direct link, in achieving superior performance in the proposed models.

VI. CONCLUSION

This paper introduces two innovative mechanisms for transforming real-valued datasets into complex-valued representations: one based on natural transformations and the other leveraging an autoencoder-driven methodology. Using these transformations, we propose RVFL-X, an enhanced extension of the Random Vector Functional Link (RVFL) network, which incorporates complex weights, activation functions, and architectures while producing real-valued outputs.

A rigorous evaluation across 80 UCI datasets, categorized into four groups, demonstrates the superior performance of RVFL-X against 10 SOTA baseline models. Detailed analyses, including accuracy, standard deviation, ranking metrics, and statistical validations such as the Friedman and Nemenyi post hoc tests, affirm the strong generalization and adaptability of RVFL-X. In every evaluation scenario, RVFL-X achieves the highest average accuracy, the lowest standard deviation, and the most favorable rankings, consistently outperforming competing methods. Furthermore, sensitivity analysis and ablation studies highlight the critical role of specific hyperparameters and architectural components in the model's success. Future extensions of this work could explore deeper and ensemble versions of RVFL-X, with potential applications in domains such as signal processing and beyond.

REFERENCES

- [1] M. A. Ganaie, M. Hu, A. K. Malik, M. Tanveer, and P. N. Suganthan, “Ensemble deep learning: A review,” *Engineering Applications of Artificial Intelligence*, vol. 115, p. 105151, 2022.
- [2] Y. Shi, K. Jiang, J. Li, Z. Qian, J. Wen, M. Yang, K. Wang, and D. Yang, “Grid-centric traffic scenario perception for autonomous driving: A comprehensive review,” *IEEE Transactions on Neural Networks and Learning Systems*, pp. 1–21, 2024. [Online]. Available: 10.1109/TNNLS.2024.3495045
- [3] M. Tanveer, T. Goel, R. Sharma, A. K. Malik, I. Beheshti, J. Del Ser, P. N. Suganthan, and C. T. Lin, “Ensemble deep learning for Alzheimer’s disease characterization and estimation,” *Nature Mental Health*, pp. 1–13, 2024.
- [4] M. Sajid, R. Sharma, I. Beheshti, M. Tanveer, and A. D. N. I., “Decoding cognitive health using machine learning: A comprehensive evaluation for diagnosis of significant memory concern,” *Wiley Interdisciplinary Reviews: Data Mining and Knowledge Discovery*, p. e1546, 2024.
- [5] M. Tanveer, M. Sajid, M. Akhtar, A. Quadir, T. Goel, A. Aimen, S. Mitra, Y.-D. Zhang, C. T. Lin, and J. D. Ser, “Fuzzy deep learning for the diagnosis of alzheimer’s disease: Approaches and challenges,” *IEEE Transactions on Fuzzy Systems*, vol. 32, no. 10, pp. 5477–5492, 2024.
- [6] A. W. Senior, R. Evans, J. Jumper, J. Kirkpatrick, L. Sifre, T. Green, C. Qin, A. Žídek, A. W. Nelson, Bridgland, and Alex, “Improved protein structure prediction using potentials from deep learning,” *Nature*, vol. 577, no. 7792, pp. 706–710, 2020.

[7] M. Gori and A. Tesi, “On the problem of local minima in backpropagation,” *IEEE Transactions on Pattern Analysis and Machine Intelligence*, vol. 14, pp. 76–86, 1992.

[8] W. F. Schmidt, M. A. Kraaijveld, and R. P. Duin, “Feed forward neural networks with random weights,” in *International Conference on Pattern Recognition*. IEEE Computer Society Press, 1992, pp. 1–1.

[9] P. N. Suganthan and R. Katuwal, “On the origins of randomization-based feedforward neural networks,” *Applied Soft Computing*, vol. 105, p. 107239, 2021.

[10] Y.-H. Pao, G.-H. Park, and D. J. Sobajic, “Learning and generalization characteristics of the random vector functional-link net,” *Neurocomputing*, vol. 6, no. 2, pp. 163–180, 1994.

[11] A. K. Malik, R. Gao, M. A. Ganaie, M. Tanveer, and P. N. Suganthan, “Random vector functional link network: Recent developments, applications, and future directions,” *Applied Soft Computing*, vol. 143, p. 110377, 2023.

[12] L. Zhang and P. N. Suganthan, “A comprehensive evaluation of random vector functional link networks,” *Information Sciences*, vol. 367, pp. 1094–1105, 2016.

[13] B. Igelnik and Y.-H. Pao, “Stochastic choice of basis functions in adaptive function approximation and the functional-link net,” *IEEE Transactions on Neural Networks*, vol. 6, no. 6, pp. 1320–1329, 1995.

[14] M. A. Ganaie, M. Sajid, A. K. Malik, and M. Tanveer, “Graph embedded intuitionistic fuzzy random vector functional link neural network for class imbalance learning,” *IEEE Transactions on Neural Networks and Learning Systems*, vol. 35, no. 9, pp. 11671–11680, 2024.

[15] A. K. Malik, M. A. Ganaie, M. Tanveer, and P. N. Suganthan, “Alzheimer’s disease diagnosis via intuitionistic fuzzy random vector functional link network,” *IEEE Transactions on Computational Social Systems*, vol. 11, no. 4, pp. 4754–4765, 2024.

[16] Y. Zhang, J. Wu, Z. Cai, B. Du, and S. Y. Philip, “An unsupervised parameter learning model for RVFL neural network,” *Neural Networks*, vol. 112, pp. 85–97, 2019.

[17] M. Sajid, A. Quadir, and M. Tanveer, “GB-RVFL: Fusion of randomized neural network and granular ball computing,” *Pattern Recognition*, vol. 159, p. 111142, 2025.

[18] M. Sajid, A. K. Malik, M. Tanveer, and P. N. Suganthan, “Neuro-fuzzy random vector functional link neural network for classification and regression problems,” *IEEE Transactions on Fuzzy Systems*, vol. 32, no. 5, pp. 2738–2749, 2024.

[19] M. Sajid, M. Tanveer, and P. N. Suganthan, “Ensemble deep random vector functional link neural network based on fuzzy inference system,” *IEEE Transactions on Fuzzy Systems*, vol. 33, no. 1, pp. 479–490, 2025.

[20] W. Dai, Y. Ao, L. Zhou, P. Zhou, and X. Wang, “Incremental learning paradigm with privileged information for random vector functional-link networks: IRVFL+,” *Neural Computing and Applications*, vol. 34, no. 9, pp. 6847–6859, 2022.

[21] N. Vuković, M. Petrović, and Z. Miljković, “A comprehensive experimental evaluation of orthogonal polynomial expanded random vector functional link neural networks for regression,” *Applied Soft Computing*, vol. 70, pp. 1083–1096, 2018.

[22] A. K. Malik, M. A. Ganaie, M. Tanveer, and P. N. Suganthan, “Extended features based random vector functional link network for classification problem,” *IEEE Transactions on Computational Social Systems*, vol. 11, no. 4, pp. 4744–4753, 2024.

[23] I. Danihelka, G. Wayne, B. Uria, N. Kalchbrenner, and A. Graves, “Associative long short-term memory,” in *International Conference on Machine Learning*. PMLR, 2016, pp. 1986–1994.

[24] S. Yadav and K. R. Jerripothula, “FCCNs: Fully complex-valued convolutional networks using complex-valued color model and loss function,” in *Proceedings of the IEEE/CVF International Conference on Computer Vision*, 2023, pp. 10689–10698.

[25] T. A. Plate, *Holographic Reduced Representation: Distributed representation for cognitive structures*. CSLI Publications Stanford, 2003, vol. 150.

[26] D. P. Reichert and T. Serre, “Neuronal synchrony in complex-valued deep networks,” *arXiv preprint arXiv:1312.6115*, 2013.

[27] G.-B. Huang, Q.-Y. Zhu, and C.-K. Siew, “Extreme learning machine: theory and applications,” *Neurocomputing*, vol. 70, no. 1-3, pp. 489–501, 2006.

[28] A. Iosifidis, A. Tefas, and I. Pitas, “Graph embedded extreme learning machine,” *IEEE Transactions on Cybernetics*, vol. 46, no. 1, pp. 311–324, 2015.

[29] M. A. Ganaie, M. Tanveer, and P. N. Suganthan, “Minimum variance embedded random vector functional link network,” in *Neural Information Processing: 27th International Conference, ICONIP 2020, Bangkok, Thailand, November 18–22, 2020, Proceedings, Part V* 27. Springer, 2020, pp. 412–419.

[30] A. Iosifidis, A. Tefas, and I. Pitas, “Minimum class variance extreme learning machine for human action recognition,” *IEEE Transactions on Circuits and Systems for Video Technology*, vol. 23, no. 11, pp. 1968–1979, 2013.

[31] D. Dua and C. Graff, “UCI machine learning repository,” 2017. [Online]. Available: <http://archive.ics.uci.edu/ml>

[32] J. Demšar, “Statistical comparisons of classifiers over multiple data sets,” *The Journal of Machine Learning Research*, vol. 7, pp. 1–30, 2006.

[33] M. Friedman, “The use of ranks to avoid the assumption of normality implicit in the analysis of variance,” *Journal of the American Statistical Association*, vol. 32, no. 200, pp. 675–701, 1937.

[34] R. L. Iman and J. M. Davenport, “Approximations of the critical region of the fbietkan statistic,” *Communications in Statistics-Theory and Methods*, vol. 9, no. 6, pp. 571–595, 1980.

[35] M. Sajid, A. K. Malik, M. Tanveer, and P. N. Suganthan,

“Neuro-fuzzy random vector functional link neural network for classification and regression problems,” *IEEE Transactions on Fuzzy Systems*, vol. 32, no. 5, pp. 2738–2749, 2024.

VII. APPENDIX

TABLE VII: Accuracy of the proposed RVFL-X models and the baseline models on C-1 category datasets.

Dataset ↓ Model →	RVFL [10]	RVFLwoDL [27]	IFRVFL [15]	GEELM-LDA [28]	GEELM-LFDA [28]	Total-var-RVFL [29]	MCVELM [30]	NF-RVFL-R [35]	NF-RVFL-K [35]	NF-RVFL-C [35]	RVFL-X-N [†]	RVFL-X-Auto [†]
acute_inflammation	100	100	100	100	100	100	100	100	100	100	100	100
acute_nephritis	100	100	100	95.8333	95.8333	100	100	100	100	100	100	100
breast_cancer_wisc	88.5653	87.9897	89.8499	86.5591	84.2724	88.704	88.8448	88.2785	88.4183	87.705	90.2785	89.9897
chess_krkv	72.0313	71.936	72.6262	76.7814	69.2351	73.7833	73.7828	82.6045	81.7008	85.2322	83.0741	84.5757
congressional_voting	63.6782	63.2184	58.8506	59.7701	54.2529	63.908	63.4483	63.908	64.1379	63.6782	64.8276	
credit_approval	85.2174	85.3623	86.5217	85.5072	85.6522	85.5072	85.5072	85.942	85.942	85.7971	85.5072	86.087
cylinder_bands	66.4154	65.8081	63.4875	67.5405	67.5385	67.7727	66.0156	68.9606	69.724	70.1294	70.1256	70.3103
echocardiogram	84.6724	83.9031	80.7692	73.2194	68.661	85.4701	85.4986	85.4416	85.4416	85.4416	85.4416	86.2108
haberman_survival	73.4902	73.8181	75.1348	55.5632	52.2898	74.4738	73.4902	75.1296	75.4574	74.146	75.4574	
ilpd_indian_liver	71.5311	72.2149	72.7277	61.7521	61.4353	72.5626	72.5508	72.3932	72.3917	72.2178	72.2384	73.4188
mammographic	79.9196	79.2978	79.7107	75.7572	73.7932	80.0237	80.2332	79.2957	79.504	79.1899	80.2321	79.1942
monks_1	83.7934	82.1654	84.6895	73.5811	71.5476	84.1538	84.8697	81.4527	82.3584	84.342	93.5151	90.8156
monks_2	80.0138	81.6804	82.6722	60.7273	57.23	85.8485	82.8499	85.8485	87.3774	87.3774	89.0041	87.5028
monks_3	91.1564	90.7912	90.0704	82.8419	74.5602	91.6986	91.8821	91.8436	91.6486	92.1744	92.9615	93.1433
pima	72.0075	72.2698	73.8282	66.401	54.0625	72.92	72.9166	73.6983	72.9174	72.6594	73.824	74.3545
pittsburg_bridges_T_OR_D	87.1905	87.1905	89.1905	82.1429	80.1905	89.1429	90.1429	90.1905	88.2381	90.1905	90.1429	90.2381
planning	71.3814	71.3814	69.8048	59.1592	61.1261	72.4925	73.048	73.018	71.9369	72.4925	73.033	
spect	68.3019	66.7925	68.3019	63.3962	62.6415	69.0566	67.9245	69.0566	69.434	68.6792	68.3019	70.1887
statlog_heart	80.3704	80	81.8519	73.7037	74.8148	81.4815	82.5926	81.4815	82.2222	81.8519	81.8519	82.2222
tic_tac_toe	88.8264	88.9278	81.4316	94.6875	79.2059	91.8521	90.0769	65.3125	68.5684	79.3216	94.5681	84.6564
vertebral_column_2clases	71.2903	70.6452	85.4839	94.8387	92.2581	72.5806	74.5161	79.0323	81.6129	80.3226	73.5484	83.871
Average	79.993	79.7806	80.3335	75.703	72.4096	81.1158	80.9615	80.6137	80.884	81.6269	<u>82.6226</u>	82.8618

TABLE VIII: Accuracy of the proposed RVFL-X models and the baseline models on C-2 category datasets.

Dataset ↓ Model →	RVFL [10]	RVFLwoDL [27]	IFRVFL [15]	GEELM-LDA [28]	GEELM-LFDA [28]	Total-var-RVFL [29]	MCVELM [30]	NF-RVFL-R [35]	NF-RVFL-K [35]	NF-RVFL-C [35]	RVFL-X-N [†]	RVFL-X-Auto [†]
adult	84.0342	83.8725	83.5438	83.422	83.1784	84.0178	83.9011	83.2992	83.5879	84.6218	84.6976	84.6259
bank	89.4051	89.4934	89.1173	89.6042	46.4966	89.6705	89.6703	89.4269	89.4492	89.9139	89.8475	89.8032
breast_cancer_wisc_diag	93.8503	92.2683	89.2719	93.1455	86.988	94.1997	93.4995	94.3751	94.3782	95.6063	95.4324	95.08
breast_cancer_wisc_prog	81.359	80.3846	78.359	62.0897	62.8462	82.359	81.8718	83.359	81.8846	80.9103	81.8718	82.8462
conn_bench_sonar_mines_rocks	62.079	60.5226	54.8316	80.5343	73.6585	64.4251	64.4251	65.8885	66.2602	63.4611	63.4959	74.007
connect_4	75.4518	75.4059	75.3407	76.7316	75.4281	75.4992	75.4459	75.4844	75.5022	76.2156	77.2266	77.0017
hill_valley	82.2603	79.7014	80.2772	76.9231	80.3846	83.6592	80.0289	82.8429	82.6732	83.0874	83.0028	85.9742
ionosphere	88.6358	86.9175	84.3581	83.2274	82.664	89.4809	88.326	88.3461	89.7626	88.9095	91.7505	90.8974
magic	78.7487	78.5279	77.5289	77.4289	78.3579	78.7171	78.7592	76.3407	76.3302	78.4017	79.3218	82.224
mushroom	96.3931	96.0735	93.9684	96.3071	98.7561	97.2919	96.7382	92.6761	95.9132	99.3351	97.7579	97.6118
oocytes_merluccius_nucleus_4d	82.2884	81.5045	79.1554	81.9957	82.7273	82.3883	82.1942	81.6021	81.7006	82.1923	83.5643	83.4605
oocytes_trisopterus_nucleus_2f	78.9419	77.5182	75.2219	78.0694	79.8889	79.6013	79.6025	79.3863	79.3779	79.9345	80.8119	82.4566
ringnorm	51.5541	51.5405	51.473	51.5541	51.5784	52.0405	51.9459	51.6081	51.6486	51.6892	51.7973	52.0135
spambase	88.546	87.0472	85.0883	88.9582	88.546	88.6116	87.4382	88.9582	88.9583	89.3931	89.2423	89.3075
Average	80.9677	80.0556	78.3954	79.9994	76.5356	81.5687	80.9891	80.971	81.2448	81.6908	<u>82.1302</u>	83.3793

TABLE IX: Accuracy of the proposed RVFL-X models and the baseline models on C-3 category datasets.

Dataset ↓ Model →	RVFL [10]	RVFLwoDL [27]	Total-var-RVFL [29]	MCVELM [30]	NF-RVFL-R [35]	NF-RVFL-K [35]	NF-RVFL-C [35]	RVFL-X-N [†]	RVFL-X-Auto [†]
annealing	89.6381	88.1918	89.1937	88.6381	86.6313	87.0782	90.8591	91.0832	91.4165
audioiology_std	69.3205	65.7564	50.3718	51.8846	71.3846	70.3718	67.8077	71.359	70.3462
balance_scale	98.4	98.4	98.56	98.56	98.4	98.24	98.24	98.72	98.56
car	72.6265	72.1057	72.6234	72.2758	70.0139	70.8337	71.0626	73.2048	72.1642
contrac	40.458	40.1183	41.3386	41.0688	41.4934	42.3673	41.5416	41.6089	45.6813
dermatology	97.5379	97.0011	97.2714	97.5417	97.5454	97.8193	97.5379	97.8119	97.5417
ecoli	60.9175	61.2116	51.0667	51.0667	60.6119	60.6277	61.5195	60.9175	62.7085
energy_y1	88.6716	88.2777	89.7106	89.0604	87.889	88.5434	89.0595	91.7927	90.7555
energy_y2	90.4932	90.4932	91.14	90.7538	89.3269	89.1928	89.8404	91.9243	92.0567
glass	37.6855	39.0808	34.4297	37.6855	42.3477	42.8239	40.4873	39.546	44.1971
hayes_roth	61.875	60.625	62.5	61.875	61.875	61.875	65	65	65
heart_cleveland	59.7268	59.377	61.0328	59.3607	61.0383	61.3388	60.0437	61.0383	61.6721
heart_va	40	40	40.5	40	41	42.5	41.5	41	41.5
iris	74.6667	74	74.6667	77.3333	73.3333	74.6667	74.6667	79.3333	85.3333
led_display	72.6	72.5	73.5	72.8	72.7	72.2	73.4	73.6	73.5
lymphography	86.4138	85.0345	86.4138	86.4368	85.7701	87.1034	88.5057	88.4368	87.7931
nursery	70.3935	70.1775	63.0093	62.8627	66.7824	66.3889	71.9444	78.1481	77.1373
pittsburg_bridges_REL_L	62.1429	63.1429	64.1429	67.0952	67.2381	69.0476	62.1905	65.1905	68.0952
seeds	89.0476	87.1429	90	89.0476	90.4762	90	90.4762	90	90.4762
soybean	87.6954	86.9579	88.4264	88.275	87.3991	88.1387	90.4723	90.3231	90.1803
teaching	69.3763	69.3763	70.6882	72.7097	70.7312	70.043	70.7097	72.0215	72.6882
vertebral_column_3clases	65.1613	65.1613	84.1935	84.1935	67.4194	69.0323	65.4839	65.8065	68.3871
yeast	57.0077	57.4117	57.4133	57.1444	55.6593	56.0005	56.8064	57.8171	57.5475
Average	71.385	70.9367	70.9649	71.203	71.6119	72.0101	72.137	<u>73.2906</u>	74.119

TABLE X: Accuracy of the proposed RVFL-X models and the baseline models on C-4 category datasets.

Dataset ↓ Model →	RVFL [10]	RVFLwoDL [27]	Total-var-RVFL [29]	MCVELM [30]	NF-RVFL-R [35]	NF-RVFL-K [35]	NF-RVFL-C [35]	RVFL-X-N [†]	RVFL-X-Auto [†]
abalone	63.4665	63.4419	63.754	63.6578	63.8253	64.1365	64.0887	63.8735	64.1126
cardiotocography_10clases	65.9924	65.2894	66.1351	66.2307	62.9851	62.8425	69.2395	71.6383	71.3568
cardiotocography_3clases	86.1733	85.5622	86.0808	85.9382	84.6213	84.2003	85.4674	86.3151	86.2216
conn_bench_vowel_deterding	95.8586	95.1515	96.1616	95.7576	87.9798	88.7879	92.2222	96.1616	96.3636
image_segmentation	87.6623	87.0996	88.3117	87.4459	83.2035	83.5931	83.6797	89.4372	89.2641
letter	80.505	79.695	80.67	79.86	61.14	63.205	81.605	82.21	82.33
low_res_spect	87.7605	86.6285	73.9852	74.1721	87.3849	87.5666	87.7605	88.8873	88.8873
ooocytes_merluccius_states_2f	91.2846	90.8948	91.8737	91.483	91.3845	91.1894	92.067	92.3625	92.4605
ooocytes_trisopterus_states_5b	87.9385	85.853	89.3647	87.8286	87.7205	87.2816	87.7175	89.2584	88.9221
optical	95.4626	94.3594	95.4626	94.8754	93.3808	94.0214	97.0107	97.4733	97.4021
page_blocks	95.4137	95.4137	95.4136	95.3952	94.6645	94.7012	94.7558	95.5963	95.5416
pendigits	98.5353	98.4716	98.6354	98.5262	92.7402	94.6233	97.5345	98.6262	98.6718
semeion	87.0673	82.4233	87.2562	83.0492	88.0726	88.5732	87.3187	90.2072	89.8925
statlog_image	95.1948	94.8918	95.6277	95.2814	91.5584	91.5584	93.0736	96.0606	96.1905
statlog_landsat	82.0513	81.4141	82.2999	81.7249	80.4196	81.3209	81.2898	82.6107	82.6884
statlog_shuttle	98.6483	98.6241	98.681	98.6793	98.6345	98.6638	98.6724	98.7224	98.7328
statlog_vehicle	82.0327	81.5593	82.0313	81.3227	79.1974	79.5475	82.2666	83.2175	83.3317
thyroid	95.625	95.4722	95.7917	95.5833	94.6667	94.7639	96.0278	96.0417	96.0278
wall_following	75.6057	75.239	75.734	75.1845	71.518	72.1223	79.583	81.1777	80.2244
waveform	86.54	85.98	86.56	86.26	86.88	86.68	87.22	87.26	87.24
waveform_noise	86.28	85.02	86.42	85.42	86.28	86.3	86.58	86.46	86.46
wine_quality_white	52.3699	52.5332	52.472	52.4103	52.4106	52.6349	53.4925	53.1047	53.4311
Average	85.3395	84.5917	84.9419	84.3676	82.7576	83.1052	85.3942	86.6683	86.6252